

## RESEARCH ARTICLE SUMMARY

## CLIMATE CHANGE

## Human influence on the seasonal cycle of tropospheric temperature

Benjamin D. Santer\*, Stephen Po-Chedley, Mark D. Zelinka, Ivana Cvijanovic, Céline Bonfils, Paul J. Durack, Qiang Fu, Jeffrey Kiehl, Carl Mears, Jeffrey Painter, Giuliana Pallotta, Susan Solomon, Frank J. Wentz, Cheng-Zhi Zou

**INTRODUCTION:** Fingerprint studies use pattern information to separate human and natural influences on climate. Most fingerprint research relies on patterns of climate change that are averaged over years or decades. Few studies probe shorter time scales. We consider here whether human influences are identifiable in the changing seasonal cycle. We focus on Earth's troposphere, which extends from the surface to roughly 16 km at the tropics and 13 km at the poles. Our interest is in  $T_{AC}$ , the geographical pattern of the amplitude of the annual cycle of tropospheric temperature. In-

formation on how  $T_{AC}$  has changed over time is available from satellite retrievals and from large multimodel ensembles of simulations.

**RATIONALE:** At least three lines of evidence suggest that human activities have affected the seasonal cycle. First, there are seasonal signals in certain human-caused external forcings, such as stratospheric ozone depletion and particulate pollution. Second, there is seasonality in some of the climate feedbacks triggered by external forcings. Third, there are widespread signals of seasonal changes in the distributions

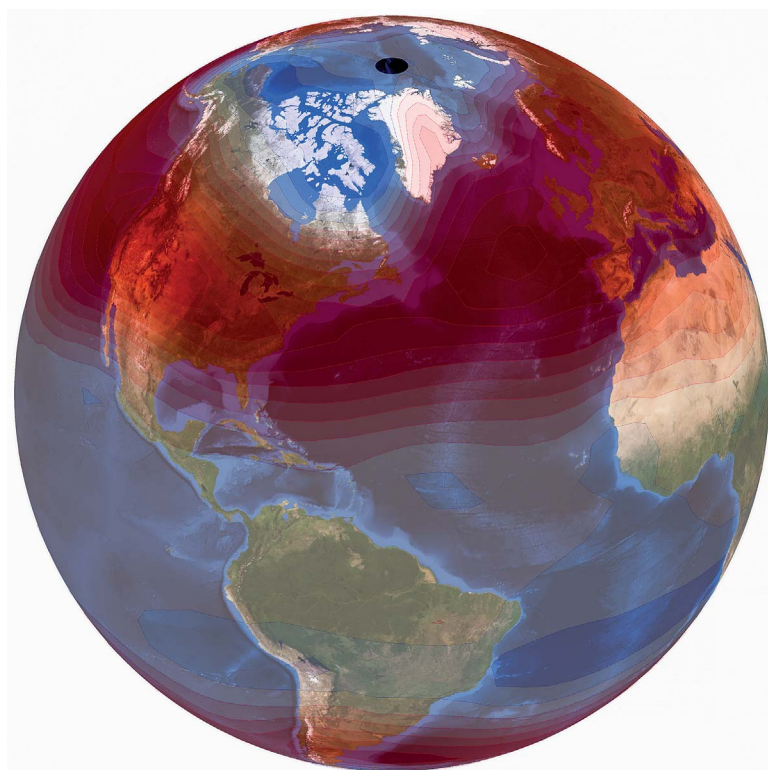
and abundances of plant and animal species. These biological signals are in part mediated by seasonal climate changes arising from global warming. All three lines of evidence provide scientific justification for performing fingerprint studies with the seasonal cycle.

**RESULTS:** The simulated response of the seasonal cycle to historical changes in human and natural factors has prominent mid-latitude increases in the amplitude of  $T_{AC}$ . These features arise from larger mid-latitude warming in the summer hemisphere, which appears to be partly attributable to continental drying. Because of land-ocean differences in heat capacity and hemispheric asymmetry in land fraction, mid-latitude increases in  $T_{AC}$  are greater in the Northern Hemisphere than in the Southern Hemisphere. Qualitatively similar large-scale patterns of annual cycle change occur in satellite tropospheric temperature data.

We applied a standard fingerprint method to determine (i) whether the pattern similarity between the model "human influence" fingerprint and satellite temperature data increases with time, and (ii) whether such an increase is significant relative to random changes in similarity between the fingerprint and patterns of natural internal variability. This method yields signal-to-noise (S/N) ratios as a function of increasing satellite record length. Fingerprint detection occurs when S/N exceeds and remains above the 1% significance threshold.

We find that the model fingerprint of externally forced seasonal cycle changes is identifiable with high statistical confidence in five out of six satellite temperature datasets. In these five datasets, S/N ratios for the 38-year satellite record vary from 2.7 to 5.8. Our positive fingerprint detection results are unaffected by the removal of all global mean information and by the exclusion of sea ice regions. On time scales for which meaningful tests are possible (one to two decades), there is no evidence that S/N ratios are spuriously inflated by a systematic model underestimate of the amplitude of observed tropospheric temperature variability.

**CONCLUSION:** Our results suggest that attribution studies with the seasonal cycle of tropospheric temperature provide powerful and novel evidence for a statistically significant human effect on Earth's climate. We hope that this finding will stimulate more detailed exploration of the seasonal signals caused by anthropogenic forcing. ■



**Trends in the amplitude of the annual cycle of tropospheric temperature.** Trends are calculated over 1979 to 2016 and are averages from a large multimodel ensemble of historical simulations. The most prominent features are pronounced mid-latitude increases in annual cycle amplitude (shown in red) in both hemispheres. Similar mid-latitude increases occur in satellite temperature data. Trends are superimposed on NASA's "blue marble" image.

## ON OUR WEBSITE

Read the full article at <http://dx.doi.org/10.1126/science.aas8806>

The list of author affiliations is available in the full article online.

\*Corresponding author. Email: [santer1@llnl.gov](mailto:santer1@llnl.gov)  
Cite this article as B. D. Santer et al., *Science* **361**, eaas8806 (2018). DOI: 10.1126/science.aas8806

## RESEARCH ARTICLE

## CLIMATE CHANGE

# Human influence on the seasonal cycle of tropospheric temperature

Benjamin D. Santer<sup>1\*</sup>, Stephen Po-Chedley<sup>1</sup>, Mark D. Zelinka<sup>1</sup>, Ivana Cvijanovic<sup>1</sup>, Céline Bonfils<sup>1</sup>, Paul J. Durack<sup>1</sup>, Qiang Fu<sup>2</sup>, Jeffrey Kiehl<sup>3</sup>, Carl Mears<sup>4</sup>, Jeffrey Painter<sup>1</sup>, Giuliana Pallotta<sup>1</sup>, Susan Solomon<sup>5</sup>, Frank J. Wentz<sup>4</sup>, Cheng-Zhi Zou<sup>6</sup>

We provide scientific evidence that a human-caused signal in the seasonal cycle of tropospheric temperature has emerged from the background noise of natural variability. Satellite data and the anthropogenic “fingerprint” predicted by climate models show common large-scale changes in geographical patterns of seasonal cycle amplitude. These common features include increases in amplitude at mid-latitudes in both hemispheres, amplitude decreases at high latitudes in the Southern Hemisphere, and small changes in the tropics. Simple physical mechanisms explain these features. The model fingerprint of seasonal cycle changes is identifiable with high statistical confidence in five out of six satellite temperature datasets. Our results suggest that attribution studies with the changing seasonal cycle provide powerful evidence for a significant human effect on Earth’s climate.

Earth’s climate is simultaneously affected by different external and internal factors. Examples of external influences are natural changes in solar irradiance and human-caused increases in atmospheric concentrations of greenhouse gases. Internal influences include a wide range of quasi-periodic natural cycles, such as the El Niño–Southern Oscillation and the Interdecadal Pacific Oscillation (IPO). Variations in these and many other internal and external factors have driven changes in historical climate.

To estimate the relative sizes of human and natural influences, analysts must separate the climate signals of multiple external factors from the noise of internal natural variability. Separation of signals and noise is a mature field of scientific inquiry, with long-standing recognition that each mode of variability and each external influence has a unique climatic signature (1). These signatures are manifest more clearly in spatial or spatiotemporal patterns than in global averages (2). Such patterns are often referred to as “fingerprints” (3).

Since the inception of climate fingerprint research in the late 1970s, scientists have used pattern recognition methods to detect unusually large changes in climate and to attribute these

changes to different external influences. Initial studies concentrated on surface and atmospheric temperature (4–6). Subsequent fingerprint research considered changes in a wide range of variables, including ocean heat content (7, 8), the hydrological cycle (9–13), atmospheric circulation (14, 15), sea ice (16), and the behavior of extreme events (17, 18). This body of work provides strong scientific evidence for a discernible human influence on global climate (19–22).

Most fingerprint studies rely on annual or decadal averages (5, 23) or attempt to understand the causes of climate change during individual seasons (4, 24). Few studies have explored whether human influences are identifiable in patterns of climate change over the seasonal cycle (16, 25–27). Multiple lines of evidence suggest that such influences exist (28, 29). First, seasonal signals occur in many external drivers of climate change, including stratospheric ozone depletion, sulfate pollution, and soot aerosols produced by biomass burning (30, 31). Second, there is seasonality in certain climate feedback mechanisms (32–35). Third, numerous scientific studies have detected significant seasonal changes in the biological world (36, 37). These biological signals are likely to be mediated (at least in part) by seasonal changes in climate.

It is therefore of interest to see whether we can identify a fingerprint of human influences on the seasonal cycle. To address this question, we use  $T_{AC}(x, t)$ , the geographical pattern of the amplitude of the annual cycle of tropospheric temperature. This pattern provides information on the differences (at grid point  $x$  and year  $t$ ) in tropospheric temperature between the warmest and coldest months of the year. We compare  $T_{AC}(x, t)$  in satellite data and in large multimodel ensembles of simulations. We also update an

analysis of  $T_{AM}(x, t)$ , the geographical pattern of annual mean changes in tropospheric temperature (38). This allows us to contrast the relative detectability of externally driven temperature signals in the annual mean and the annual cycle.

A number of previous studies have compared the consistency between simulated and observed changes in the phase and amplitude of surface temperature, and have attempted to understand the contributions these changes receive from internal variability and external forcing (26, 39–43). To date, however, no formal fingerprint study has been performed with the amplitude of the annual cycle of tropospheric temperature. Unlike surface temperature datasets, satellite measurements of tropospheric temperature have near-global coverage and no gaps in time. This is advantageous for fingerprint studies.

## Satellite and model data

The satellite temperature data analyzed here are measurements of the microwave emissions from oxygen molecules. These emissions are proportional to the temperature of broad atmospheric layers. The measurements of primary interest in this study are the temperatures of the mid- to upper troposphere (TMT) and of the lower troposphere (TLT). TMT receives a contribution from stratospheric cooling, which hampers assessment of the warming of the troposphere. We use a standard regression-based approach to correct TMT for stratospheric influence (44, 45). This correction method requires satellite information on the temperature of the lower stratosphere (TLS), which we also discuss briefly. In the following, TMT denotes model and satellite data from which stratospheric influence has been removed (46).

Satellite atmospheric temperature data with near-global coverage were available from three research groups: Remote Sensing Systems (RSS), the NOAA Center for Satellite Applications and Research (STAR), and the University of Alabama at Huntsville (UAH) (47–49). Use of information from multiple groups allows us to assess the sensitivity of anthropogenic fingerprint identification to current observational uncertainties. Because all three research groups provide both older and newer dataset versions, we can also evaluate the sensitivity of our fingerprint results to changes over time in the data-processing decisions made by each group. These decisions are necessary in order to correct for nonclimatic artifacts in the satellite data.

Artifacts arise from factors such as orbital decay (50) and orbital drift (51). Orbital changes affect the measurements of microwave emissions, primarily because of gradual shifts in the time of day at which measurements are made. Adjustments for shifts in measurement time are large and involve many subjective choices (47–49, 51–56). Additional adjustments to the raw data are required to account for drifts in the onboard calibration of the microwave measurements (49, 55, 57, 58) and for the transition in the late 1990s between earlier and more advanced versions of the microwave sounders (47). In the

<sup>1</sup>Program for Climate Model Diagnosis and Intercomparison (PCMDI), Lawrence Livermore National Laboratory, Livermore, CA 94550, USA. <sup>2</sup>Department of Atmospheric Sciences, University of Washington, Seattle, WA 98195, USA. <sup>3</sup>Earth and Planetary Sciences, University of California, Santa Cruz, CA 95064, USA. <sup>4</sup>Remote Sensing Systems, Santa Rosa, CA 95401, USA. <sup>5</sup>Earth, Atmospheric, and Planetary Sciences, Massachusetts Institute of Technology, Cambridge, MA 02139, USA. <sup>6</sup>Center for Satellite Applications and Research, NOAA/NESDIS, College Park, MD 20740, USA. \*Corresponding author. Email: santer1@llnl.gov



case of the UAH TMT data, there is evidence that this transition has not been adequately accounted for, resulting in abrupt, nonclimatic changes in the amplitude of the annual cycle of TMT (see below).

To facilitate comparison with observations, we calculated “synthetic” satellite temperatures (38) using different types of model simulations. We obtained information on internal climate variability from pre-industrial control runs with no year-to-year changes in external influences. Estimates of the response to combined changes in human and natural external factors were derived from simulations of historical climate (HIST) and 21st-century climate. The latter experiments assume evolution of greenhouse gases, particulate pollution, and other external influences under

Representative Concentration Pathway 8.5 (RCP8.5) (59). Splicing of the HIST and RCP8.5 simulations (HIST+8.5) allows comparison of simulations and observations over 38 complete years of satellite record (1979 to 2016). We also analyze integrations with historical changes in anthropogenic external influences only (ANTHRO). All simulations were performed under phase 5 of the Coupled Model Intercomparison Program (CMIP5) (60).

### Climatological annual mean and annual cycle

We first examine whether the HIST+8.5 simulations successfully capture key features of the observed climatological patterns of TMT, both for the annual mean and the annual cycle.

Reliable representation of these patterns enhances confidence in the credibility of our fingerprint results.

TMT samples temperature changes over an atmospheric layer extending from the surface to roughly 16 km in the tropics and 13 km at the poles (53). Despite the large vertical extent of this layer, TMT retains an imprint of land-versus-ocean differences, which is clearly evident in the tropics (Fig. 1, left column). This land-ocean imprint is primarily related to the ocean's greater heat capacity. Because there are no large continental land masses at mid-latitudes in the Southern Hemisphere, TMT is more zonally uniform between 40° and 70°S than between 40° and 70°N. These features of the observed mean state are well represented in the multimodel average.

The climatological annual cycle of TMT also reveals the influence of land-ocean differences (Fig. 1, right column). In the Northern Hemisphere, the largest differences between the warmest and coldest months occur over the eastern margin of Eurasia. The annual cycle amplitude near western continental margins is reduced by eastward advection of warmer oceanic air masses during winter (39, 42) and cooler oceanic air masses in summer. Because of the hemispheric asymmetry in land fraction, annual cycle amplitudes at mid-latitudes are smaller in the Southern Hemisphere (42). In the deep tropics, where there is little seasonal variation in incoming solar radiation, the annual cycle in TMT is less than 1°C. As in the case of the annual mean, the multimodel average replicates these basic features of the observed climatological annual cycle.

The seasonal change in TMT over each individual year has annual and semiannual components. CMIP5 models successfully reproduce large-scale features of the observed partitioning

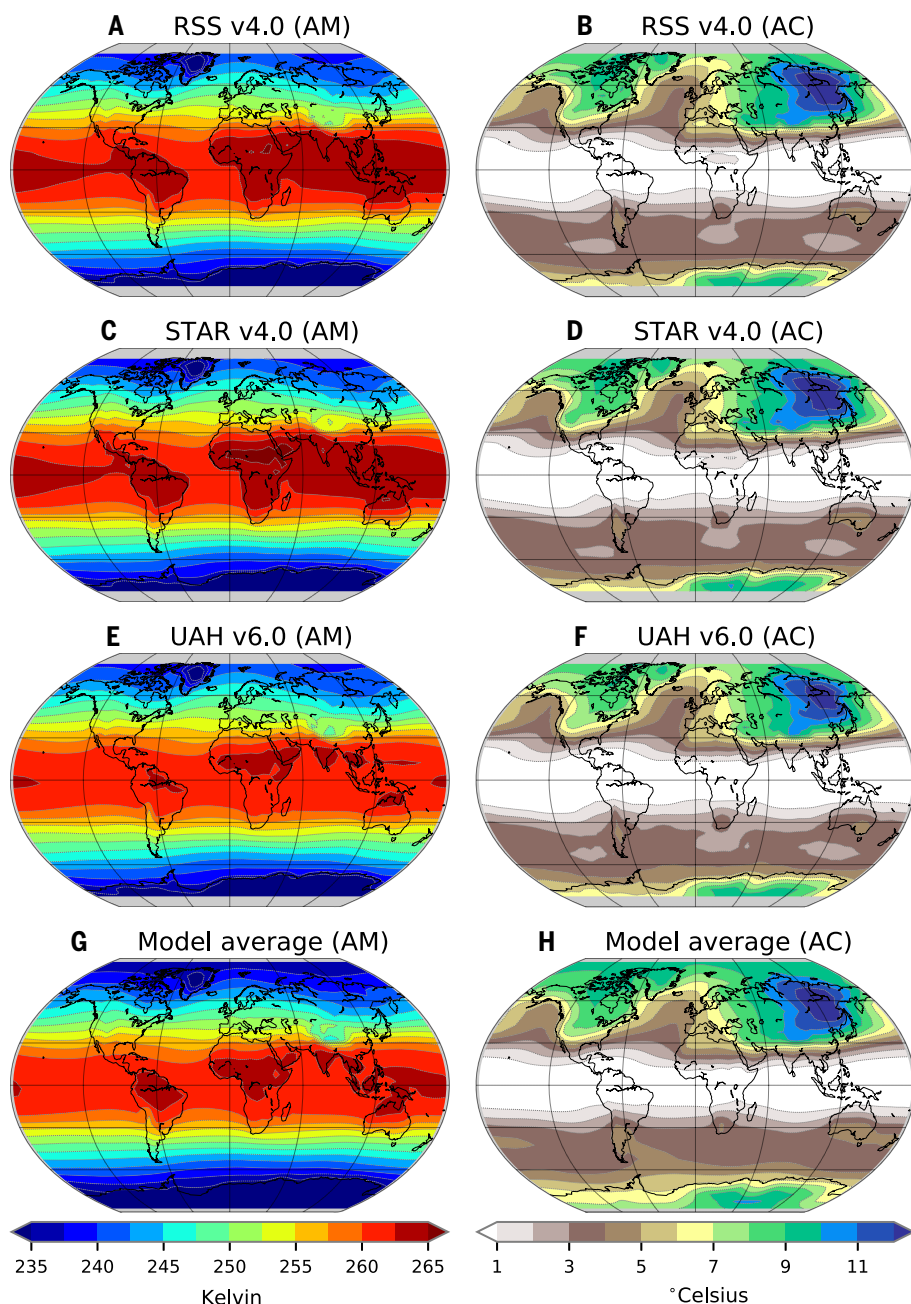


**Fig. 1. Climatological annual mean (left column) and annual cycle (right column) of the temperature of the mid- to upper troposphere (TMT).** (A to F) Results from the latest versions of the RSS, STAR, and UAH satellite datasets. (G and H) Multimodel average of synthetic TMT data from simulations with combined anthropogenic and natural external forcing (HIST+8.5). Simulations were performed with 37 different CMIP5 models. TMT is corrected for the influence of stratospheric cooling. Climatologies were calculated over the 38-year period from 1979 to 2016 and are displayed on a common 5° × 5° latitude/longitude grid. At each grid point and for each year, the annual cycle is the amplitude of the first harmonic of the 12 monthly mean values of corrected TMT. In the tropics, climatological annual mean TMT in UAH is more zonally symmetric than in either RSS or STAR. Differences between the three sets of observational results are noticeably smaller for the climatological pattern of the annual cycle than for the annual mean.

between these components. In the extratropics and polar regions, incoming solar radiation is dominated by the annual cycle, which drives the large annual cycle in TMT (fig. S1). The semi-annual cycle in TMT is largest close to the equator, where there is a double peak in incoming solar radiation over each year. Small-scale discrepancies between the models and observations occur in the equatorial Pacific, Atlantic, and Indonesian regions, where the semiannual cycle explains less seasonal variance in the multimodel average than in satellite data. These regional discrepancies are evident in most individual CMIP5 models (fig. S2). Their causes are unclear.

### Geographical trend patterns

Next, we analyze geographical patterns of trends in the annual mean and annual cycle of TMT. Consider the observed annual mean trends first (Fig. 2, left column). Satellite TMT data show large-scale tropospheric warming over the period 1979 to 2016 (47, 56, 61, 62). Annual mean cooling is restricted to small portions of the troposphere poleward of 60°S. Other common features of the observations are Arctic amplification of warming (62–64), secondary warming maxima between 30° and 40°N and in the Southern Hemisphere subtropics, and reduced warming near the Aleutian and Icelandic Lows.

The multimodel average captures some but not all of these features. As in the satellite data, there is global-scale tropospheric warming, with greater warming in the Northern Hemisphere. Unlike the observations, however, the multimodel average has no high-latitude cooling in the Southern Hemisphere. Individual models yield a large range of negative and positive TMT trends in this region (fig. S3). This range is due to multiple factors. Examples include model performance in representing stratospheric ozone changes over Antarctica (31, 38, 65, 66) and in capturing changes in circulation and upwelling in the Southern Ocean (64, 67).

Model-versus-observed trend differences are also partly due to internal variability (62, 68). The model results in Fig. 2 are averages over individual HIST+8.5 realizations (each with their own random sequence of internal climate variability) and over individual models. Averaging reduces the size of simulated internal climate variability, yielding a smoother estimate of the tropospheric temperature response to external forcing. In the real world, only one sequence of internal variability is overlaid on the TMT response to external forcing. We therefore expect observed trend patterns to be noisier. This is particularly noticeable in mid-latitude  $T_{AC}(x,t)$  trends, where satellite data show wave-train features and multimodel average changes are more zonal. Individual models are capable of replicating such wave-train features (fig. S4).

Considerable scientific attention has been devoted to the tropical troposphere, where simulated warming is greater than observed (47, 53, 56, 62, 69, 70). Possible reasons for overestimated tropical warming include model errors in climate sensitivity (71), different phas-

ing of natural internal variability in the model runs relative to the real world (72–77), and residual errors in the satellite data (47, 78). Scientific attention has also focused on forcing errors in the HIST+8.5 simulations, as well as on the omission (and/or inaccurate representation) of certain external cooling influences that affected observed climate in the early 21st century (65, 77, 79–84). The claim that overestimation of warming is solely due to a large error in climate model sensitivity (71) has been tested elsewhere and is not credible (85, 86).

Trends in the amplitude of the annual cycle of TMT are characterized by a number of large-scale features that are common to the satellite datasets and the HIST+8.5 multimodel average (Fig. 2, right column). These features include amplitude increases in mid-latitudes of both hemispheres, smaller positive and negative changes over large areas of the tropics, and decreases over the Indian monsoon region. Amplitude decreases poleward of 60°S are another feature that is common to the multimodel average and observations (except UAH v6.0).

Poleward of 60°N, all satellite datasets have substantial decreases in the amplitude of the annual cycle of TMT. This decrease in  $T_{AC}(x,t)$  arises in part from greater warming in Arctic winter than in Arctic summer. At the surface, greater winter warming is primarily related to differences in the seasonal timing of feedbacks associated with sea ice retreat (35). The ice-albedo feedback yields greater summertime heat storage in the Arctic Ocean, which in turn leads to increased wintertime sea ice retreat and increased wintertime heat release from the ocean to the polar atmosphere (35). This seasonality in sea ice trends and ocean heat storage is accompanied by seasonal changes in cloud and water vapor feedbacks and in ocean and atmospheric heat transport (35, 63, 87). All of these processes affect not only surface temperature, but also the vertical structure of tropospheric temperature.

Although roughly one-third of the individual models successfully capture the observed decrease in  $T_{AC}(x,t)$  over the Arctic, model-average  $T_{AC}(x,t)$  trends in this region are close to zero. This discrepancy between satellite and model-average Arctic  $T_{AC}(x,t)$  trends may have a number of different causes. One possible cause is that most CMIP5 models underestimate observed Arctic sea ice loss (35, 88, 89). The model average is therefore likely to underestimate the observed seasonal warming of the Arctic associated with ocean heat storage and release, cloud and water vapor feedbacks, and heat transport by the atmosphere and the ocean (35, 63, 87). Other possible causes of discrepancies between satellite and model Arctic  $T_{AC}(x,t)$  trends include model representation of influences from outside the Arctic (90, 91), model errors in the deposition of aerosols on snow and sea ice (92), differences in the phasing of internal variability in the real world and in the HIST+8.5 simulations (93), and the fact that synthetic microwave sounding unit (MSU) temperatures do not account for surface

emissivity changes associated with sea ice retreat in the HIST+8.5 runs (46).

### Trends in zonal mean data

Calculating trends in zonally averaged data reduces the observed “pattern noise” in Fig. 2, A to F, and highlights areas of large-scale agreement and disagreement between simulations and observations. In Fig. 3, we show trends in zonal mean  $T_{AM}(x,t)$  and  $T_{AC}(x,t)$  for the stratosphere, mid- to upper troposphere, and lower troposphere. This allows us to study the vertical coherence of the TMT results from the previous section.

Consider the annual mean results first (Fig. 3, left column). Trends in zonal means are characterized by hemispheric asymmetry, with greater tropospheric warming (and smaller stratospheric cooling) in the Northern Hemisphere than in the Southern Hemisphere. These hemispheric asymmetries in temperature change are evident in all three atmospheric layers. They are common to the models and satellite data, and are more pronounced in the observations (38). In the tropics, multimodel average trends in annual mean TMT and TLT are always more positive than in the observations, and the model average overestimation of warming extends throughout the Southern Hemisphere. In contrast, most individual models underestimate the observed Arctic amplification of tropospheric warming (Fig. 3, C and E).

A prominent feature of observed trends in zonal mean  $T_{AC}(x,t)$  is mid-latitude “ridging” in both hemispheres (Fig. 3, right column). In the troposphere, these mid-latitude ridges represent large increases in the annual cycle of temperature. In the stratosphere, where there are decreases in the zonal mean amplitude of the annual temperature cycle at almost all latitudes, the observed mid-latitude ridging signifies smaller amplitude decreases. This ridging behavior is captured by the multimodel average, but only for TMT and TLT. Mid-latitude increases in the annual cycle are larger in satellite data than in the multimodel average. In the Northern Hemisphere, the observed mid-latitude increase in annual cycle amplitude is consistently displaced poleward relative to the model results.

The trends in zonal mean  $T_{AC}(x,t)$  also have interesting features at high latitudes. All satellite datasets exhibit large decreases in annual cycle amplitude poleward of 60°N; decreases are evident in both the stratosphere and the troposphere. Model average changes poleward of 60°N are noticeably weaker, and there is substantial model disagreement in the sign and size of trends. This holds for TLS, TMT, and TLT. At high latitudes in the Southern Hemisphere, however, most models yield a decrease in the amplitude of the annual cycle of TMT, consistent with most satellite datasets. This common decrease in  $T_{AC}(x,t)$  is not driven by the same seasonal phasing of TMT changes (see below).

It is of interest to compare older and newer versions of satellite TMT datasets (Fig. 3). For trends in zonal mean  $T_{AM}(x,t)$ , differences



between the dataset versions of an individual group are generally smaller than between-group differences. This is not true for trends in zonal mean  $T_{AC}(x,t)$ . Poleward of roughly  $55^{\circ}\text{S}$ , the amplitude of the annual cycle of TMT decreases in the earlier version of the UAH dataset (v5.6) but increases in the latest version (v6.0). The trend difference between UAH v5.6 and v6.0 appears to be related to changes in how UAH analysts treated the 1998 transition between MSUs and advanced MSUs. At this transition, the time series of differences between UAH v5.6 and v6.0 exhibits an abrupt change in the amplitude of the seasonal cycle. Differences between earlier and current versions of the RSS and STAR datasets do not show this apparent discontinuity. The large changes in  $T_{AC}(x,t)$  between the two UAH dataset versions have important implications for anthropogenic fingerprint detection (see below).

### Seasonality of temperature changes

To gain insight into the seasonality of the temperature changes driving the trends in the amplitude of the annual cycle, we analyze the trends in zonal mean TMT over 1979 to 2016 as a function of month (Fig. 4). The multimodel average trends are generally large relative to intermodel differences in the trends, indicating that the seasonal structure of the model TMT changes is robust over most latitude bands (except poleward of  $\sim 60^{\circ}\text{S}$ ).

Consider first the prominent mid-latitude increases in the annual cycle of tropospheric temperature, which are common to both the multimodel average and the satellite data (Fig. 3D). Although mid-latitude warming occurs throughout the year, it is more pronounced in the summer hemisphere, with a warming minimum in the winter hemisphere (particularly at roughly  $55^{\circ}\text{N}$  in February). This seasonality in tropospheric warming largely explains the mid-latitude increases in  $T_{AC}(x,t)$  in model and satellite data. Qualitatively similar results have been obtained elsewhere for uncorrected TMT (62).

There are also some noticeable differences between the simulated and observed seasonal warming patterns in Fig. 4. In the tropics, the satellite data show greater seasonality of warming. Poleward of  $70^{\circ}\text{N}$ , the pronounced observed warming maximum between January through March is absent from the multimodel average (62). A further difference between the model and observational trend patterns occurs between roughly  $30^{\circ}$  and  $45^{\circ}\text{N}$ , where the satellite data show a warming maximum from January through March. This maximum is not reproduced by the multimodel average. It is unclear whether such small-scale differences are physically meaningful or are purely due to the observational “pattern noise” described above (62, 68).

Recall that poleward of  $55^{\circ}\text{S}$ , the amplitude of the annual cycle of TMT decreased over the satellite era in the multimodel average and in all satellite datasets except UAH v6.0 (Fig. 3D). In the latest versions of the RSS and STAR data, this

decrease is due to the phasing of maximum cooling in December-January and maximum warming in October-November. The multimodel average captures part of the observed seasonal phasing of TMT changes (reduced warming in December-January) but has maximum warming in June-August rather than in October-November. Such mismatches in phasing may be partly due to model errors in representing observed Antarctic ozone changes (38, 65, 66). A model with more realistic representation of the nonlinear temporal

evolution of stratospheric ozone changes (94) yields better agreement with the observed seasonal phasing of TMT trends over the Antarctic continent (62).

### Fingerprint analysis

We used a standard method to determine whether the model fingerprints in response to external forcing are statistically identifiable in satellite tropospheric temperature data (1, 38). Although we calculated fingerprints from both

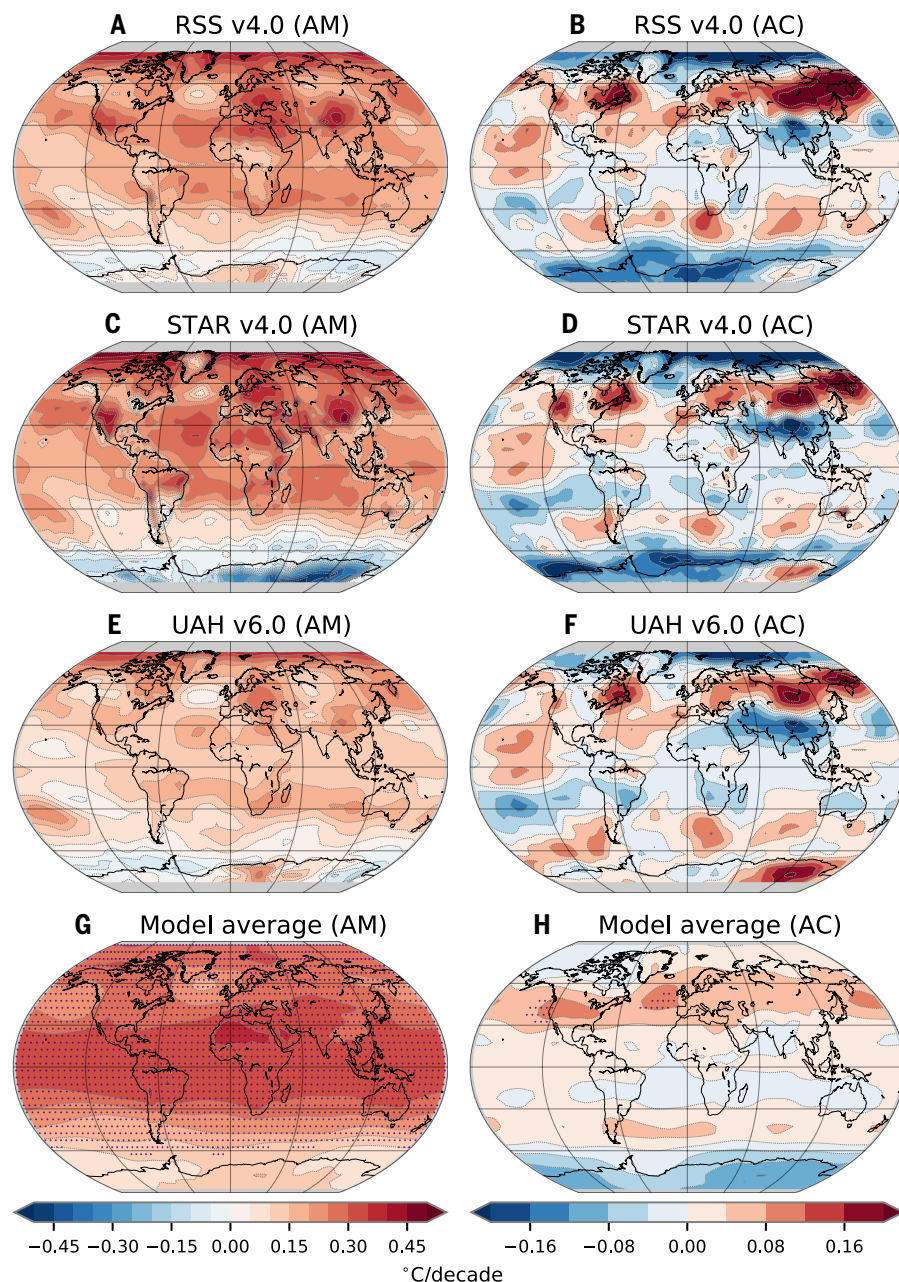


**Fig. 2. Trends over 1979 to 2016 in the annual mean (left column) and annual cycle (right column) of corrected TMT.** Satellite TMT data (A to F) and model TMT data (G and H) are described in Fig. 1. The stippling in (G) and (H) denotes grid points where the multimodel average trend in the annual mean or annual cycle exceeds the between-model standard deviation of the trend by at least a factor of 1.5. For the annual mean, tropical warming in UAH is noticeably reduced relative to RSS and STAR. Results are displayed on a common  $5^{\circ} \times 5^{\circ}$  latitude/longitude grid.

the ANTHRO and HIST+8.5 simulations, we focus here on the HIST+8.5 fingerprints (46). Whether we use the ANTHRO or HIST+8.5 fingerprints has minimal influence on the main findings of our study. The annual mean and annual cycle fingerprints we seek,  $F_{AM}(x)$  and  $F_{AC}(x)$ , are the leading empirical orthogonal function (EOF) of the multi-model average anomalies of the annual mean and annual cycle of tropospheric temperature. Fingerprints were calculated over 1979 to 2016 and are shown in fig. S5, A and B.

An important assumption in our fingerprint method is that these normalized fingerprint patterns are time-invariant (31, 94). To test this assumption, we analyzed trends in  $T_{AM}(x,t)$  and  $T_{AC}(x,t)$  over four different 38-year periods. In

the annual mean case, a distinctive pattern of tropospheric warming emerges as the size of net anthropogenic forcing increases over time (fig. S6, left column). Key features of this pattern are maximum warming in the tropics, greater warming in the Northern Hemisphere than in the Southern Hemisphere, and local warming minima in the vicinity of the Aleutian and Icelandic Lows. Although the amplitude of this annual mean warming pattern increases with increasing forcing, the pattern itself is very similar in the final three 38-year analysis periods.

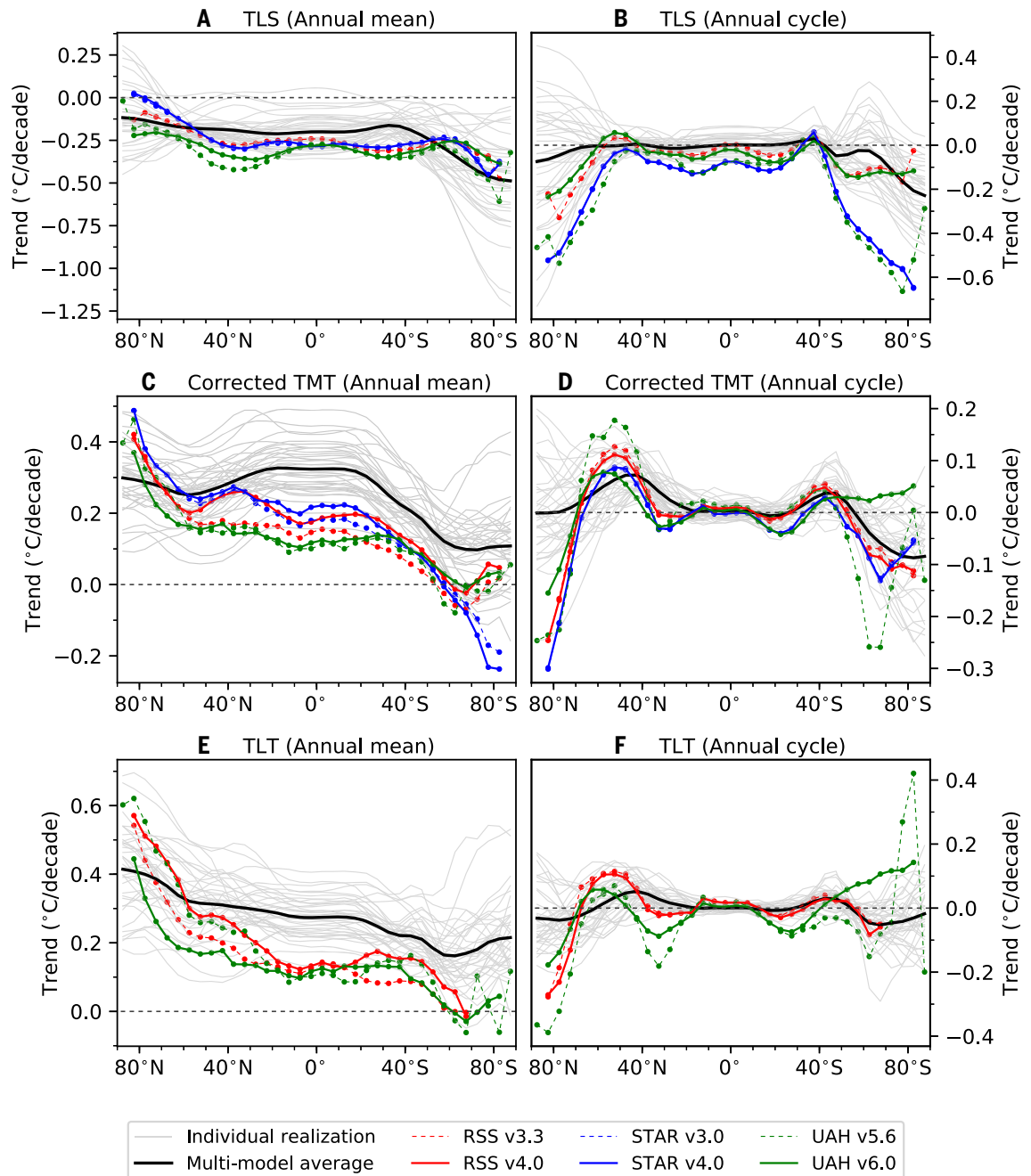
The same holds for the spatial pattern of trends in  $T_{AC}(x,t)$  (fig. S6, right column). The above-described “ridging” pattern, characterized by pronounced mid-latitude increases in the

amplitude of the annual cycle, is established by the second analysis period (1979 to 2016) and remains relatively stable in the mid- to late 21st century. The only major change in the pattern of TMT trends is over the Antarctic continent, where 21st-century changes in  $T_{AC}(x,t)$  are likely to be affected by recovery from stratospheric ozone depletion (31, 94). Over most of the globe, however, the “satellite era” fingerprints used here are representative of the fingerprint patterns that would be obtained with analysis periods in the mid- or late 21st century.

We seek to determine (i) whether the pattern similarity between the HIST+8.5 fingerprints and satellite temperature data increases with time, and (ii) whether such an increase is significant

**Fig. 3. Zonal mean trends over 1979 to 2016 in the annual mean (left column) and annual cycle (right column) of simulated and observed atmospheric temperature.**

Results are for the temperature of the lower stratosphere (TLS) (A and B), the corrected TMT (C and D), and the temperature of the lower troposphere (TLT) (E and F). The thin gray lines are the HIST+8.5 results from 37 different CMIP5 models. Where TMT was available for multiple HIST+8.5 realizations, ensemble means are shown. For the satellite datasets, trends are given for both older and most recent dataset versions (dashed and solid colored lines, respectively). TLT is not available from STAR, and RSS v4.0 data were not available for TLS at the time this study was performed.



relative to random changes in similarity between the fingerprint and patterns of natural internal variability. To address these questions, we compare the HIST+8.5 fingerprints with temperature change patterns from the satellite temperature datasets and from model control runs. This comparison yields “signal” and “noise” time series, respectively, which we use to calculate S/N ratios (Fig. 5) (46). We stipulate that fingerprint detection occurs at the trend length  $L_D$  for which the S/N ratio first exceeds a nominal 1% significance threshold, and then remains above that threshold for all trend lengths  $L > L_D$ .

We also show S/N results for calculations that do not involve any observational data. Noise time series are computed as described above. In computing the signal time series, however, satellite data are replaced with time-varying temperature changes in individual model HIST+8.5 simulations. These “model only” results help us

to assess whether the strength and time evolution of the fingerprint is similar in model and satellite data.

It is of interest to determine whether identification of a model-predicted anthropogenic fingerprint is primarily due to large global mean temperature changes, with little contribution from true spatial pattern similarity. To address this issue, we performed S/N calculations with and without the global mean. In the latter case, the global mean change in temperature at each time  $t$  is removed from all model and satellite datasets prior to fingerprint estimation and S/N analysis. We refer to these cases subsequently as “mean included” and “mean removed.”

Consider the annual mean results first. In the “mean included” case, the model HIST+8.5 fingerprint is identifiable with high statistical confidence in all six satellite datasets (Fig. 5A). Over the 38-year satellite record, S/N ratios range from 4.4 to 7.3, depending on the choice of

satellite dataset. The credibility of these S/N ratios rests on the assumption that the model control runs analyzed here provide reliable estimates of the true (but uncertain) statistical properties of “real-world” natural internal variability on 30- to 40-year time scales. The adequacy of this assumption is difficult to assess with the single available realization of the 38-year satellite temperature record (85, 95, 96). On shorter time scales for which meaningful variability tests are possible (one to two decades), there is no evidence that our S/N ratios are spuriously inflated by a systematic model underestimate of the amplitude of observed TMT variability (see fig. S7).

For trends longer than roughly 25 years, model S/N ratios are systematically larger than S/N ratios calculated with annual mean satellite TMT data. These longer trends sample temperature changes in the early 21st century, when the HIST+8.5 simulations have known deficiencies in their representation of certain external cooling influences.

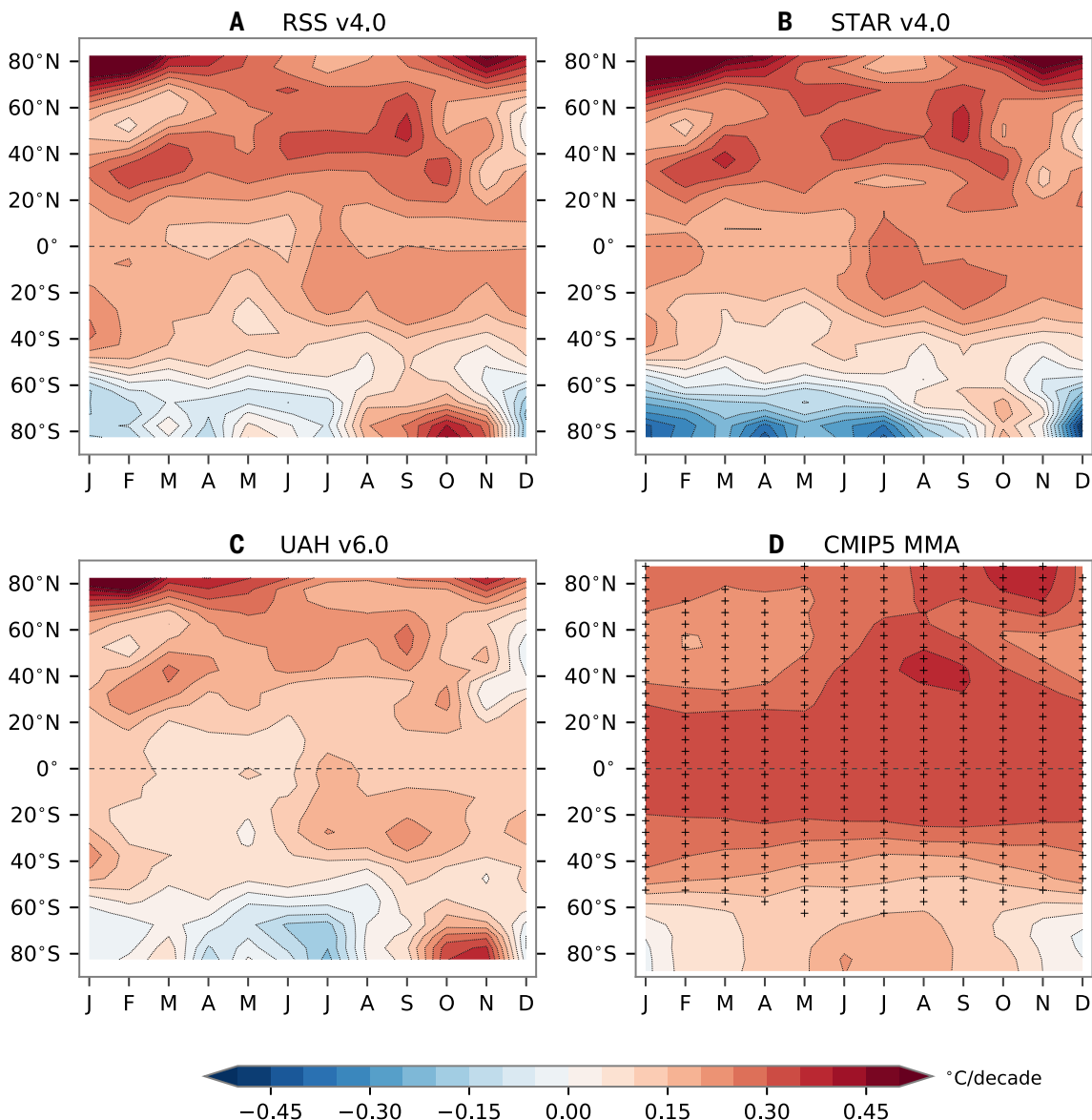


**Fig. 4. Zonal mean trends over 1979 to 2016 in monthly averages of corrected TMT.**

Results are for the latest versions of the RSS, STAR, and UAH satellite datasets [(A to C), respectively] and for the multimodel average of the CMIP5 HIST+8.5 simulations (D). The plus symbols in (D) indicate multimodel average trends that exceed the between-model standard deviation of the zonal-mean monthly mean trend by at least a factor of 1.5. As in Fig. 3, all satellite and model temperature data were transformed to a common  $5^\circ \times 5^\circ$  latitude/longitude grid prior to zonal averaging.



Examples include omission of the post-2000 cooling caused by a succession of moderate volcanic eruptions (80, 81, 83, 84, 97–99) and by the unusually long and low minimum in solar irradiance during the last solar cycle (100).

The early 21st century was also a period during which the real world experienced internally generated cooling influences. These were due to the post-1998 transition to a negative phase of the IPO and to the fortuitous phasing of other modes of natural variability (72–77). Coupled models have random sequences of internal variability and are not expected to replicate the observed

phasing of internally generated temperature fluctuations, except by chance.

When global mean changes are removed, “model only” S/N ratios are not systematically larger than observationally based S/N results. The HIST+8.5 fingerprint of annual mean TMT changes is still consistently identifiable in all satellite datasets (Fig. 5B). S/N ratios range from 2.3 to 6.4 for calculations spanning the full satellite record. These values are smaller than in the “mean included” case but are still above the 1% significance threshold. This demonstrates that successful detection of the HIST+8.5 fingerprint

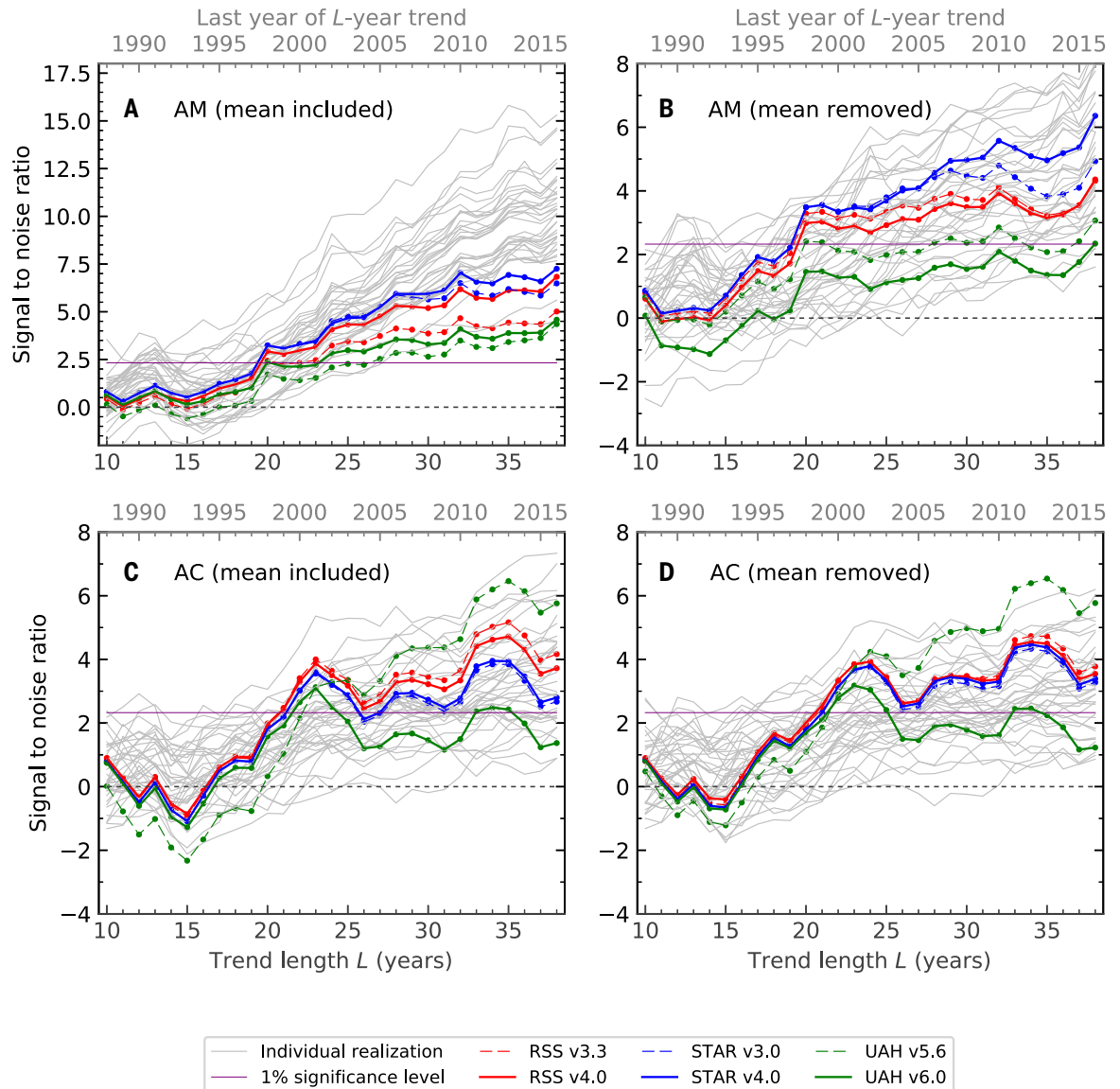
in observations is not driven by global mean changes alone: The large S/N ratios in the “mean included” case carry appreciable spatial pattern information, such as common hemispheric asymmetry in warming (see Figs. 2 and 3C).

S/N ratios for the annual cycle do not differ markedly between the “mean included” and the “mean removed” cases (Fig. 5, C and D). This is because global mean changes in  $T_{AC}(x,t)$  are relatively small. Most of the signal is in the zonal mean pattern of amplitude changes (Fig. 3D). The HIST+8.5 annual cycle fingerprint is identifiable in five out of six satellite datasets,

**Fig. 5. Signal-to-noise (S/N) analysis of changes in the geographical patterns of corrected TMT.**

Results are for patterns of change in the annual mean (A and B) and annual cycle (C and D) of TMT. The analysis was performed on a  $10^\circ \times 10^\circ$  latitude/longitude grid; the latitudinal extent of the domain was from  $80^\circ\text{N}$  to  $80^\circ\text{S}$ . Results in (A) and (C) rely on model and satellite temperature datasets that include  $\langle T(t) \rangle$ , the spatially averaged temperature in year  $t$ . In (B) and (D),  $\langle T(t) \rangle$  was subtracted from all HIST+8.5 simulations, control runs, and satellite datasets prior to S/N analysis. The searched-for annual mean and annual cycle fingerprints,  $F_{AM}(x)$  and  $F_{AC}(x)$ , are estimated from the multimodel average annual mean and annual cycle results.  $F_{AM}(x)$  and  $F_{AC}(x)$  are time-invariant. A pattern similarity metric is applied to estimate the strength of each

fingerprint in time-varying satellite datasets and in long model simulations of natural internal variability. This yields “signal” and “noise” time series, respectively (46). For each satellite dataset, we fit  $L$ -year trends to the signal time series to obtain the numerator of the S/N ratio. The first signal trend is over the 10-year period from 1979 to 1988, the second is over the 11-year period from 1979 to 1989, and the final 38-year signal trend is over the full satellite record (1979 to 2016). The denominator of the S/N ratio is the standard deviation of the multimodel sampling distribution of  $L$ -year noise



trends, calculated using 7200 years of temperature data from 36 CMIP5 control runs. The time scale of the noise trends matches the time scale of the signal: Signal trends over 1979 to 1988 are compared with the standard deviation of the sampling distribution of 10-year noise trends, etc. “Model only” results also shown (the 37 thin gray lines in each panel). The “model only” signal time series are calculated by comparing individual model HIST+8.5 simulations with the multimodel average AM and AC fingerprints. The horizontal purple line is the nominal 1% significance level.



irrespective of whether global mean changes are retained or removed. In these five datasets, S/N ratios for the 38-year satellite record vary from 2.7 to 5.8 for the “mean included” case, and from 3.3 to 5.8 for the “mean removed” data. The only dataset in which  $F_{AC}(x)$  cannot be detected is UAH v6.0. Recall that poleward of 55°S, UAH v6.0 has zonal mean  $T_{AC}(x,t)$  trends of opposite sign to trends in all other satellite datasets and in the multimodel average (Fig. 3D). This discrepancy must contribute to the null result obtained with the UAH v6.0 data.

There are concerns regarding how well satellite TMT data represent true tropospheric temperature change in high-latitude regions experiencing a substantial decrease in sea ice extent (107). To address these concerns, we repeated our “standard” S/N analysis of corrected TMT, which was performed over 80°N to 80°S, for a 60°N to 60°S domain. S/N ratios are similar for the larger and smaller regions (compare Fig. 5 and fig. S8). This indicates that exclusion of areas with large changes in sea ice extent has minimal impact on our findings.

Why do we obtain detection of the HIST+8.5 fingerprints for both the annual mean and annual cycle of TMT? Comparison of the fingerprints with the leading modes of natural internal variability helps to address this question (fig. S5). In the annual mean case,  $F_{AM}(x)$  is characterized by large-scale, hemispherically asymmetric tropospheric warming. In contrast, the dominant modes of variability in annual mean TMT do not have the same sign everywhere, are smaller in scale, and exhibit anticorrelated variability between different broad zonal bands (and between Eurasia and North America). Patterns of annual mean trends in satellite TMT data are more similar to  $F_{AM}(x)$  than to the leading noise modes (compare Fig. 2, A, C, and E, and fig. S5).

Because of these pattern differences and similarities, the fingerprint acts as a filter, removing internal variability that is spatially dissimilar to  $F_{AM}(x)$  while “passing” observed TMT changes. The same applies in the annual cycle case. The pronounced zonal structure of  $F_{AC}(x)$  captures many features of the observed annual cycle changes, but differs markedly from the smaller-scale (and less zonal) variability patterns estimated from the control runs.

We performed a similar S/N analysis for the lower troposphere (fig. S9). Annual mean TLT results are consistent with those obtained for TMT:  $F_{AM}(x)$  is robustly identifiable in all versions of the RSS and UAH annual mean TLT data, in both the “mean included” and “mean removed” cases. For the annual cycle, however, the TLT results are markedly different. Although  $F_{AC}(x)$  was identifiable in five out of six observed TMT datasets, it could not be detected in any of the satellite TLT datasets. Reasons for this discrepancy are discussed below.

## Discussion

Mid-latitude increases in the amplitude of the annual cycle of TMT are prominent features of both the satellite observations and the HIST+8.5

simulations (Fig. 3D). What physical mechanisms might explain these features? Specifically, we seek to understand why the mid-latitude increase in  $T_{AC}(x,t)$  is larger in the Northern than in the Southern Hemisphere, and why mid-latitude tropospheric warming is greater in the summer hemisphere. We address these questions using zonal mean surface temperature changes in the HIST+8.5 simulations. We analyze these changes over the climatological seasonal cycle and over the period 1979 to 2016.

Consider the seasonal cycle first. At mid-latitudes, the seasonal cycle is larger in the Northern than in the Southern Hemisphere (fig. S10A). This asymmetry arises for two reasons: (i) Land has smaller effective heat capacity than ocean, and therefore warms more than ocean in response to spring-to-summer insolation changes, and cools more in fall-to-winter; and (ii) the mid-latitude land fraction is larger in the Northern than in the Southern Hemisphere. Because of advection of heat fluxes between mid-latitude land and ocean, hemispheric asymmetry is not restricted to the combined “land and ocean” zonal means; it is also manifest in zonal mean surface temperatures calculated using land and ocean grid points only (fig. S10, C and E, respectively).

Land-ocean differences in heat capacity and hemispheric differences in land fraction also influence the long-term surface temperature response to anthropogenic forcing. Zonal mean surface temperature trends over the satellite era show pronounced hemispheric asymmetry, with greater mid-latitude warming in the Northern than in the Southern Hemisphere (fig. S10, B, D, and F). The maximum mid-latitude surface warming occurs in the summer hemisphere, particularly in boreal summer in the “land only” zonal averages (fig. S10D).

One possible explanation for the latter result is progressive summertime drying of the mid-latitude continental land surface in response to anthropogenic greenhouse gas increases (102, 103). This drying yields an increase in sensible heat flux from the land surface to the atmosphere (102). Recent research suggests that in boreal summer, the mid-latitude continental drying signal predicted by CMIP5 models is statistically identifiable in observed soil moisture and near-surface relative humidity datasets (104). There are, however, still substantial uncertainties in this drying and warming signal. These uncertainties are partly related to model biases in summertime land surface temperature (105).

The same basic physical mechanisms drive hemispheric asymmetry in the latitude-height structure of tropospheric temperature changes (fig. S11). This holds for temperature changes over the climatological seasonal cycle and for temperature trends over the satellite era. To highlight hemispheric asymmetries, we show differences between August and February—the months during which the warmest tropical tropospheric temperatures are furthest northward in boreal summer and furthest southward in austral summer (fig. S12).

Consider the seasonal cycle first (fig. S11A). Below roughly 200 hPa, the August-minus-February tropospheric temperature differences at mid-latitudes are markedly larger in the Northern than in the Southern Hemisphere. The August-minus-February tropospheric temperature trend differences exhibit similar asymmetry and amplify with increasing height, consistent with a moist adiabatic lapse rate (106, 107) (fig. S11B). The maximum trend differences are at roughly 200 hPa and at 40°N and 40°S. These features are qualitatively similar to the latitude-height pattern of changes in the amplitude of the annual cycle in response to CO<sub>2</sub> doubling (42).

We turn next to the question of why we can detect the anthropogenic  $F_{AC}(x)$  fingerprint in TMT but not in TLT. Because of amplification by moist thermodynamic processes (69, 70, 106), the greenhouse gas-forced signal in  $T_{AC}(x,t)$  should be larger in corrected TMT than in TLT (42). This is in fact the case. In the HIST+8.5 simulations, the fingerprint  $F_{AC}(x)$  explains 37% of the overall space-time variance of the multimodel average TMT changes. For TLT, the variance explained by  $F_{AC}(x)$  is substantially smaller (22%; fig. S13A). It is this larger signal in TMT that explains the differences between signal detection results for TMT and TLT. Differences in noise do not appear to play a major role—the partitioning of internally generated variability as a function of EOF number is similar for TMT and TLT (fig. S13B).

The basic physical processes described above are unlikely to be the only drivers of the pattern and amplitude of the annual cycle changes in Fig. 3D. Over the Antarctic continent, stratospheric and tropospheric cooling arising from human-caused ozone changes can exert seasonal influence on high- and mid-latitude Southern Hemisphere atmospheric circulation and temperature (62, 108, 109). This influence occurs primarily via the Southern Annular Mode (SAM) (110) but may also operate through more complex interactions among ozone loss, planetary wave activity, and seasonal tropospheric circulation (108). Greenhouse gas forcing also induces SAM responses, which are expected to strengthen over the 21st century (111).

A number of previous studies have reported that the tropics are expanding poleward (109, 112–115). This is in accord with basic theory linking global warming to increases in static stability and to a poleward shift in the latitude of baroclinic instability (116). Tropical expansion in response to warming is also manifest in satellite observations of tropospheric temperature change (112, 114) and in a wide range of simulations performed with models of varying complexity (107, 117). Expectations of temperature changes arising from tropical expansion, derived from theory, models, and observations (107, 109, 112, 114, 116, 117), appear to be consistent with the mid-latitude  $T_{AC}(x,t)$  changes in Fig. 3D. Further work is required to understand and quantify the contributions to these  $T_{AC}(x,t)$  changes from tropical expansion and the physical mechanisms described here.

Recently, it has been claimed that climate scientists cannot reliably quantify human and natural contributions to global warming (118, 119). Such claims are not supported either by the present work or by related climate change detection and attribution studies (4–8, 11, 21, 22, 38). We find here that for annual mean TMT, the estimated S/N ratios exceed 4.4 for temperature changes over the 38-year satellite record. This translates to odds of roughly 5 in 1 million of obtaining the annual mean S/N ratios by natural variability alone. To negate the positive detection of an anthropogenic fingerprint in satellite  $T_{AM}(x,t)$  datasets, the model-based estimates of natural variability used here to calculate S/N ratios would have to underestimate real-world low-frequency variability by a factor of 2 or more. For tropospheric temperature, there is no evidence that an error of this magnitude exists. On average, CMIP5 models appear to overestimate the observed natural variability of TMT on decadal time scales (38).

Across the most recent versions of observational TMT datasets, structural uncertainty in the geographical pattern of trends appears to be smaller for annual cycle amplitude than for the annual mean (Fig. 2, A to F). This is advantageous for detection and attribution studies. Furthermore, we note that the annual cycle of tropospheric temperature is not routinely used in model evaluation. It is highly unlikely, therefore, that the positive fingerprint identification results obtained here for the annual cycle could be due to model tuning. The best explanation for these results is that basic physics and basic physical mechanisms are driving the large-scale changes in  $T_{AC}(x,t)$ . For tropospheric temperature, a human-caused signal is now evident in the seasonal cycle itself.

## REFERENCES AND NOTES

1. K. Hasselmann, *On the Signal-To-Noise Problem in Atmospheric Response Studies* (Royal Meteorological Society, London, 1979), pp. 251–259.
2. G. R. North, K. Y. Kim, S. S. P. Shen, J. W. Hardin, Detection of forced climate signals. Part I: Filter theory. *J. Clim.* **8**, 401–408 (1995). doi: [10.1175/1520-0442\(1995\)008<0401:DOFCSF>2.0.CO;2](https://doi.org/10.1175/1520-0442(1995)008<0401:DOFCSF>2.0.CO;2)
3. M. C. MacCracken, H. Moses, *First Detection of Carbon Dioxide Effects: Workshop Summary* (1982); [www.osti.gov/scitech/biblio/5590773](http://www.osti.gov/scitech/biblio/5590773).
4. G. C. Hegerl *et al.*, Detecting greenhouse-gas-induced climate change with an optimal fingerprint method. *J. Clim.* **9**, 2281–2306 (1996). doi: [10.1175/1520-0442\(1996\)009<2281:DGGICC>2.0.CO;2](https://doi.org/10.1175/1520-0442(1996)009<2281:DGGICC>2.0.CO;2)
5. B. D. Santer *et al.*, A search for human influences on the thermal structure of the atmosphere. *Nature* **382**, 39–46 (1996). doi: [10.1038/382039a0](https://doi.org/10.1038/382039a0)
6. S. F. B. Tett, J. F. B. Mitchell, D. E. Parker, M. R. Allen, Human influence on the atmospheric vertical temperature structure: Detection and observations. *Science* **274**, 1170–1173 (1996). doi: [10.1126/science.274.5290.1170](https://doi.org/10.1126/science.274.5290.1170); pmid: 8895461
7. T. P. Barnett *et al.*, Penetration of human-induced warming into the world's oceans. *Science* **309**, 284–287 (2005). doi: [10.1126/science.1112418](https://doi.org/10.1126/science.1112418); pmid: 15933161
8. P. J. Gleckler *et al.*, Human-induced global ocean warming on multidecadal time scales. *Nat. Clim. Change* **2**, 524–529 (2012). doi: [10.1038/nclimate1553](https://doi.org/10.1038/nclimate1553)
9. B. D. Santer *et al.*, Incorporating model quality information in climate change detection and attribution studies. *Proc. Natl. Acad. Sci. U.S.A.* **106**, 14778–14783 (2009). doi: [10.1073/pnas.0901736106](https://doi.org/10.1073/pnas.0901736106); pmid: 19706477
10. K. Marvel, C. Bonfils, Identifying external influences on global precipitation. *Proc. Natl. Acad. Sci. U.S.A.* **110**, 19301–19306 (2013). doi: [10.1073/pnas.1314382110](https://doi.org/10.1073/pnas.1314382110); pmid: 24218561
11. P. A. Stott, R. T. Sutton, D. M. Smith, Detection and attribution of Atlantic salinity changes. *Geophys. Res. Lett.* **35**, L21702 (2008). doi: [10.1029/2008GL035874](https://doi.org/10.1029/2008GL035874)
12. D. W. Pierce, P. J. Gleckler, T. P. Barnett, B. D. Santer, P. J. Durack, The fingerprint of human-induced changes in the ocean's salinity and temperature fields. *Geophys. Res. Lett.* **39**, L21704 (2012). doi: [10.1029/2012GL053389](https://doi.org/10.1029/2012GL053389)
13. L. Terray *et al.*, Near-surface salinity as Nature's rain gauge to detect human influence on the tropical water cycle. *J. Clim.* **25**, 958–977 (2012). doi: [10.1175/JCLI-D-10-05025.1](https://doi.org/10.1175/JCLI-D-10-05025.1)
14. N. P. Gillett, J. Fyfe, D. Parker, Attribution of observed sea level pressure trends to greenhouse gas, aerosol, and ozone changes. *Geophys. Res. Lett.* **40**, 2302–2306 (2013). doi: [10.1002/grl.50500](https://doi.org/10.1002/grl.50500)
15. N. Christidis, P. A. Stott, Changes in the geopotential height at 500 hPa under the influence of external climate forcings. *Geophys. Res. Lett.* **42**, 10798–10,806 (2015). doi: [10.1002/2015GL066669](https://doi.org/10.1002/2015GL066669)
16. S. K. Min, X. Zhang, F. W. Zwiers, T. Agnew, Human influence on Arctic sea ice detectable from early 1990s onwards. *Geophys. Res. Lett.* **35**, L21701 (2008). doi: [10.1029/2008GL035725](https://doi.org/10.1029/2008GL035725)
17. P. A. Stott, D. A. Stone, M. R. Allen, Human contribution to the European heatwave of 2003. *Nature* **432**, 610–614 (2004). doi: [10.1038/nature03089](https://doi.org/10.1038/nature03089); pmid: 15577907
18. P. A. Stott *et al.*, Attribution of extreme weather and climate-related events. *WIREs Clim. Change* **7**, 23–41 (2016). doi: [10.1002/wcc.380](https://doi.org/10.1002/wcc.380); pmid: 26877771
19. B. D. Santer, T. M. L. Wigley, T. P. Barnett, E. Anyamba, in *Climate Change 1995: The Science of Climate Change. Contribution of Working Group I to the Second Assessment Report of the Intergovernmental Panel on Climate Change*, J. T. Houghton *et al.*, Eds. (Cambridge University Press, 1995), pp. 407–443.
20. J. F. B. Mitchell, D. J. Karoly, in *Climate Change 2001: The Scientific Basis. Contribution of Working Group I to the Third Assessment Report of the Intergovernmental Panel on Climate Change*, J. T. Houghton *et al.*, Eds. (Cambridge Univ. Press, 2001), pp. 695–738.
21. G. C. Hegerl *et al.*, in *Climate Change 2007: The Physical Science Basis. Contribution of Working Group I to the Fourth Assessment Report of the Intergovernmental Panel on Climate Change*, S. Solomon *et al.*, Eds. (Cambridge Univ. Press, 2007), pp. 663–745.
22. N. L. Bindoff *et al.*, in *Climate Change 2013: The Physical Science Basis. Contribution of Working Group I to the Fifth Assessment Report of the Intergovernmental Panel on Climate Change*, T. F. Stocker *et al.*, Eds. (Cambridge Univ. Press, 2013), pp. 867–952.
23. M. R. Allen, S. F. B. Tett, Checking for model consistency in optimal fingerprinting. *Clim. Dyn.* **15**, 419–434 (1999). doi: [10.1007/s003820050291](https://doi.org/10.1007/s003820050291)
24. D. Polson, G. C. Hegerl, X. Zhang, T. J. Osborn, Causes of robust seasonal land precipitation changes. *J. Clim.* **26**, 6679–6697 (2013). doi: [10.1175/JCLI-D-12-00474.1](https://doi.org/10.1175/JCLI-D-12-00474.1)
25. B. D. Santer, T. M. L. Wigley, M. E. Schlesinger, P. D. Jones, *Multivariate Methods for the Detection of Greenhouse-Gas-Induced Climate Change* (Elsevier, 1990), pp. 511–536.
26. C. Qian, X. Zhang, Human influences on changes in the temperature seasonality in mid-to high-latitude land areas. *J. Clim.* **28**, 5908–5921 (2015). doi: [10.1175/JCLI-D-14-00821.1](https://doi.org/10.1175/JCLI-D-14-00821.1)
27. K. Marvel *et al.*, Observed and projected changes to the precipitation annual cycle. *J. Clim.* **30**, 4983–4995 (2017). doi: [10.1175/JCLI-D-16-0572.1](https://doi.org/10.1175/JCLI-D-16-0572.1)
28. D. J. Thomson, The seasons, global temperature, and precession. *Science* **268**, 59–68 (1995). doi: [10.1126/science.268.5207.59](https://doi.org/10.1126/science.268.5207.59); pmid: 17755231
29. M. E. Mann, J. Park, Greenhouse warming and changes in the seasonal cycle of temperature: Models versus observations. *Geophys. Res. Lett.* **23**, 1111–1114 (1996). doi: [10.1029/96GL01066](https://doi.org/10.1029/96GL01066)
30. S. Solomon, Stratospheric ozone depletion: A review of concepts and history. *Rev. Geophys.* **37**, 275–316 (1999). doi: [10.1029/1999RG900008](https://doi.org/10.1029/1999RG900008)
31. S. Solomon *et al.*, Emergence of healing in the Antarctic ozone layer. *Science* **353**, 269–274 (2016). doi: [10.1126/science.aae0061](https://doi.org/10.1126/science.aae0061); pmid: 27365314
32. A. Hall, X. Qu, Using the current seasonal cycle to constrain snow albedo feedback in future climate change. *Geophys. Res. Lett.* **33**, L03502 (2006). doi: [10.1029/2005GL025127](https://doi.org/10.1029/2005GL025127)
33. P. C. Taylor, R. G. Ellingson, M. Cai, Seasonal variations of climate feedbacks in the NCAR CCSM3. *J. Clim.* **24**, 3433–3444 (2011). doi: [10.1175/JCLI3862.1](https://doi.org/10.1175/JCLI3862.1)
34. C. J. W. Bonfils *et al.*, On the influence of shrub height and expansion on northern high latitude climate. *Environ. Res. Lett.* **7**, 015503 (2012). doi: [10.1088/1748-9326/7/1/015503](https://doi.org/10.1088/1748-9326/7/1/015503)
35. R. Bintanja, E. C. van der Linden, The changing seasonal climate in the Arctic. *Sci. Rep.* **3**, 1556 (2013). doi: [10.1038/srep01556](https://doi.org/10.1038/srep01556); pmid: 23532038
36. C. Parmesan, G. Yohe, A globally coherent fingerprint of climate change impacts across natural systems. *Nature* **421**, 37–42 (2003). doi: [10.1038/nature01286](https://doi.org/10.1038/nature01286); pmid: 12511946
37. T. L. Root, D. P. MacMynowski, M. D. Mastrandrea, S. H. Schneider, Human-modified temperatures induce species changes: Joint attribution. *Proc. Natl. Acad. Sci. U.S.A.* **102**, 7465–7469 (2005). doi: [10.1073/pnas.0502286102](https://doi.org/10.1073/pnas.0502286102); pmid: 15899975
38. B. D. Santer *et al.*, Identifying human influences on atmospheric temperature. *Proc. Natl. Acad. Sci. U.S.A.* **110**, 26–33 (2013). doi: [10.1073/pnas.1210514109](https://doi.org/10.1073/pnas.1210514109); pmid: 23197824
39. A. R. Stine, P. Huybers, I. Y. Fung, Changes in the phase of the annual cycle of surface temperature. *Nature* **457**, 435–440 (2009). doi: [10.1038/nature07675](https://doi.org/10.1038/nature07675); pmid: 19158790
40. A. R. Stine, P. Huybers, Changes in the seasonal cycle of temperature and atmospheric circulation. *J. Clim.* **25**, 7362–7380 (2012). doi: [10.1175/JCLI-D-11-00470.1](https://doi.org/10.1175/JCLI-D-11-00470.1)
41. J. G. Dwyer, M. Biasutti, A. H. Sobel, Projected changes in the seasonal cycle of surface temperature. *J. Clim.* **25**, 6359–6374 (2012). doi: [10.1175/JCLI-D-11-00741.1](https://doi.org/10.1175/JCLI-D-11-00741.1)
42. A. Donohoe, D. S. Battisti, The seasonal cycle of atmospheric heating and temperature. *J. Clim.* **26**, 4962–4980 (2013). doi: [10.1175/JCLI-D-12-00713.1](https://doi.org/10.1175/JCLI-D-12-00713.1)
43. S. Nigam, N. P. Thomas, A. Ruiz-Barradas, S. J. Weaver, Striking seasonality in the secular warming of the northern continents: Structure and mechanisms. *J. Clim.* **30**, 6521–6541 (2017). doi: [10.1175/JCLI-D-16-0757.1](https://doi.org/10.1175/JCLI-D-16-0757.1)
44. Q. Fu, C. M. Johanson, S. G. Warren, D. J. Seidel, Contribution of stratospheric cooling to satellite-inferred tropospheric temperature trends. *Nature* **429**, 55–58 (2004). doi: [10.1038/nature02524](https://doi.org/10.1038/nature02524); pmid: 15129277
45. Q. Fu, C. M. Johanson, Stratospheric influences on MSU-derived tropospheric temperature trends: A direct error analysis. *J. Clim.* **17**, 4636–4640 (2004). doi: [10.1175/JCLI-3267.1](https://doi.org/10.1175/JCLI-3267.1)
46. See supplementary materials.
47. C. Mears, F. J. Wentz, Sensitivity of satellite-derived tropospheric temperature trends to the diurnal cycle adjustment. *J. Clim.* **29**, 3629–3646 (2016). doi: [10.1175/JCLI-D-15-0744.1](https://doi.org/10.1175/JCLI-D-15-0744.1)
48. J. R. Christy, W. B. Norris, R. W. Spencer, J. J. Hnilo, Tropospheric temperature change since 1979 from tropical radiosonde and satellite measurements. *J. Geophys. Res.* **112**, D06102 (2007). doi: [10.1029/2005JD006881](https://doi.org/10.1029/2005JD006881)
49. C.-Z. Zou, W. Wang, Inter-satellite calibration of AMSU-A observations for weather and climate applications. *J. Geophys. Res.* **116**, D23113 (2011). doi: [10.1029/2011JD016205](https://doi.org/10.1029/2011JD016205)
50. F. J. Wentz, M. Schabel, Effects of orbital decay on satellite-derived lower-tropospheric temperature trends. *Nature* **394**, 661–664 (1998). doi: [10.1038/29267](https://doi.org/10.1038/29267)
51. C. A. Mears, F. J. Wentz, The effect of diurnal correction on satellite-derived lower tropospheric temperature. *Science* **309**, 1548–1551 (2005). doi: [10.1126/science.1114772](https://doi.org/10.1126/science.1114772); pmid: 16141071
52. C. Mears, F. J. Wentz, P. Thorne, D. Bernie, Assessing uncertainty in estimates of atmospheric temperature changes from MSU and AMSU using a Monte-Carlo technique. *J. Geophys. Res.* **116**, D08112 (2011). doi: [10.1029/2010JD014954](https://doi.org/10.1029/2010JD014954)
53. T. R. Karl, S. J. Hassol, C. D. Miller, W. L. Murray, Eds., *Temperature Trends in the Lower Atmosphere: Steps for Understanding and Reconciling Differences. A Report by the U.S. Climate Change Science Program and the Subcommittee on Global Change Research* (National Oceanic and Atmospheric Administration, 2006).
54. C.-Z. Zou *et al.*, Recalibration of microwave sounding unit for climate studies using simultaneous nadir overpasses. *J. Geophys. Res.* **111**, D19114 (2006). doi: [10.1029/2005JD006798](https://doi.org/10.1029/2005JD006798)

55. C.-Z. Zou, M. Gao, M. Goldberg, Error structure and atmospheric temperature trends in observations from the Microwave Sounding Unit. *J. Clim.* **22**, 1661–1681 (2009). doi: [10.1175/2008JCLI2233.1](https://doi.org/10.1175/2008JCLI2233.1)
56. S. Po-Chedley, T. J. Thorsen, Q. Fu, Removing diurnal cycle contamination in satellitederived tropospheric temperatures: Understanding tropical tropospheric trend discrepancies. *J. Clim.* **28**, 2274–2290 (2015). doi: [10.1175/JCLI-D-13-00767.1](https://doi.org/10.1175/JCLI-D-13-00767.1)
57. C. A. Mears, M. C. Schabel, F. J. Wentz, A reanalysis of the MSU channel 2 tropospheric temperature record. *J. Clim.* **16**, 3650–3664 (2003). doi: [10.1175/1520-0442\(2003\)016<3650:AROTMC>2.0.CO;2](https://doi.org/10.1175/1520-0442(2003)016<3650:AROTMC>2.0.CO;2)
58. S. Po-Chedley, Q. Fu, A bias in the mid-tropospheric channel warm target factor on the NOAA-9 Microwave Sounding Unit. *J. Atmos. Ocean. Technol.* **29**, 646–652 (2012). doi: [10.1175/JTECH-D-11-00147.1](https://doi.org/10.1175/JTECH-D-11-00147.1)
59. M. Meinshausen *et al.*, The RCP greenhouse gas concentrations and their extensions from 1765 to 2300. *Clim. Change* **109**, 213–241 (2011). doi: [10.1007/s10584-011-0156-z](https://doi.org/10.1007/s10584-011-0156-z)
60. K. E. Taylor, R. J. Stouffer, G. A. Meehl, An overview of CMIP5 and the experiment design. *Bull. Am. Meteorol. Soc.* **93**, 485–498 (2012). doi: [10.1175/BAMS-D-11-00094.1](https://doi.org/10.1175/BAMS-D-11-00094.1)
61. B. D. Santer *et al.*, Comparing tropospheric warming in climate models and satellite data. *J. Clim.* **30**, 373 (2017). doi: [10.1175/JCLI-D-16-0333.1](https://doi.org/10.1175/JCLI-D-16-0333.1)
62. W. J. Randel *et al.*, Troposphere-stratosphere temperature trends derived from satellite data compared with ensemble simulations from WACCM. *J. Geophys. Res.* **122**, 9651 (2017). doi: [10.1002/2017JD027158](https://doi.org/10.1002/2017JD027158)
63. M. C. Serreze, R. G. Barry, Processes and impacts of Arctic amplification: A research synthesis. *Global Planet. Change* **77**, 85–96 (2011). doi: [10.1016/j.gloplacha.2011.03.004](https://doi.org/10.1016/j.gloplacha.2011.03.004)
64. J. Marshall *et al.*, The ocean's role in polar climate change: Asymmetric Arctic and Antarctic responses to greenhouse gas and ozone forcing. *Philos. Trans. R. Soc. A* **372**, 20130040 (2014). doi: [10.1098/rsta.2013.0040](https://doi.org/10.1098/rsta.2013.0040)
65. S. Solomon, P. J. Young, B. Hassler, Uncertainties in the evolution of stratospheric ozone and implications for recent temperature changes in the tropical lower stratosphere. *Geophys. Res. Lett.* **39**, L17706 (2012). doi: [10.1029/2012GL052723](https://doi.org/10.1029/2012GL052723)
66. V. Eyring *et al.*, Long-term ozone changes ozone and associated climate impacts in CMIP5 simulations. *J. Geophys. Res.* **118**, 5029–5060 (2013). doi: [10.1002/jgrd.50316](https://doi.org/10.1002/jgrd.50316)
67. K. C. Armour, J. Marshall, J. R. Scott, A. Donohoe, E. R. Newsom, Southern Ocean warming delayed by circumpolar upwelling and equatorward transport. *Nat. Geosci.* **9**, 549–554 (2016). doi: [10.1038/ngeo2731](https://doi.org/10.1038/ngeo2731)
68. J. C. Fyfe *et al.*, Large near-term projected snowpack loss over the western United States. *Nat. Commun.* **8**, 14996 (2017). pmid: [28418406](https://pubmed.ncbi.nlm.nih.gov/28418406/)
69. B. D. Santer *et al.*, Amplification of surface temperature trends and variability in the tropical atmosphere. *Science* **309**, 1551–1556 (2005). doi: [10.1126/science.1114867](https://doi.org/10.1126/science.1114867); pmid: [16099951](https://pubmed.ncbi.nlm.nih.gov/16099951/)
70. Q. Fu, S. Manabe, C. M. Johanson, On the warming in the tropical upper troposphere: Models versus observations. *Geophys. Res. Lett.* **38**, L15704 (2011). doi: [10.1029/2011GL048101](https://doi.org/10.1029/2011GL048101)
71. J. R. Christy, Testimony in Hearing before the Subcommittee on Energy and Power, Committee on Energy and Commerce, House of Representatives, March 8, 2011. Available online at [www.nsstc.uah.edu/users/john.christy/christy/ChristyJR\\_Written\\_EP\\_110308.pdf](http://www.nsstc.uah.edu/users/john.christy/christy/ChristyJR_Written_EP_110308.pdf).
72. Y. Kosaka, S.-P. Xie, Recent global-warming hiatus tied to equatorial Pacific surface cooling. *Nature* **501**, 403–407 (2013). doi: [10.1038/nature12534](https://doi.org/10.1038/nature12534); pmid: [23995690](https://pubmed.ncbi.nlm.nih.gov/23995690/)
73. M. H. England *et al.*, Recent intensification of wind-driven circulation in the Pacific and the ongoing warming hiatus. *Nat. Clim. Change* **4**, 222–227 (2014). doi: [10.1038/nclimate2106](https://doi.org/10.1038/nclimate2106)
74. G. A. Meehl, J. M. Arblaster, J. T. Fasullo, A. Hu, K. E. Trenberth, Model-based evidence of deep-ocean heat uptake during surface-temperature hiatus periods. *Nat. Clim. Change* **1**, 360–364 (2011). doi: [10.1038/nclimate229](https://doi.org/10.1038/nclimate229)
75. G. A. Meehl, H. Teng, J. M. Arblaster, Climate model simulation of the observed early-2000s hiatus of global warming. *Nat. Clim. Change* **4**, 898–902 (2014). doi: [10.1038/nclimate2357](https://doi.org/10.1038/nclimate2357)
76. B. A. Steinman, M. E. Mann, S. K. Miller, Atlantic and Pacific multidecadal oscillations and Northern Hemisphere temperatures. *Science* **347**, 988–991 (2015). doi: [10.1126/science.1257856](https://doi.org/10.1126/science.1257856); pmid: [25722410](https://pubmed.ncbi.nlm.nih.gov/25722410/)
77. J. C. Fyfe *et al.*, Making sense of the early-2000s warming slowdown. *Nat. Clim. Change* **6**, 224–228 (2016). doi: [10.1038/nclimate2938](https://doi.org/10.1038/nclimate2938)
78. C. Mears, F. J. Wentz, A satellite-derived lower-tropospheric atmospheric temperature dataset using an optimized adjustment for diurnal effects. *J. Clim.* **30**, 7695–7718 (2017). doi: [10.1175/JCLI-D-16-0768.1](https://doi.org/10.1175/JCLI-D-16-0768.1)
79. S. Solomon *et al.*, Contributions of stratospheric water vapor to decadal changes in the rate of global warming. *Science* **327**, 1219–1223 (2010). doi: [10.1126/science.1182488](https://doi.org/10.1126/science.1182488); pmid: [20110466](https://pubmed.ncbi.nlm.nih.gov/20110466/)
80. S. Solomon *et al.*, The persistently variable “background” stratospheric aerosol layer and global climate change. *Science* **333**, 866–870 (2011). doi: [10.1126/science.1206027](https://doi.org/10.1126/science.1206027); pmid: [21778361](https://pubmed.ncbi.nlm.nih.gov/21778361/)
81. J. M. Haywood, A. Jones, G. S. Jones, The impact of volcanic eruptions in the period 2000–2013 on global mean temperature trends evaluated in the HadGEM2-ES climate model. *Atmos. Sci. Lett.* **15**, 92–96 (2013). doi: [10.1002/asl2.471](https://doi.org/10.1002/asl2.471)
82. G. A. Schmidt, D. T. Shindell, K. Tsigaridis, Reconciling warming trends. *Nat. Geosci.* **7**, 158–160 (2014). doi: [10.1038/ngeo2105](https://doi.org/10.1038/ngeo2105)
83. D. A. Ridley *et al.*, Total volcanic stratospheric aerosol optical depths and implications for global climate change. *Geophys. Res. Lett.* **41**, 7763–7769 (2014). doi: [10.1002/2014GL061541](https://doi.org/10.1002/2014GL061541)
84. D. M. Smith *et al.*, Role of volcanic and anthropogenic aerosols in the recent global surface warming slowdown. *Nat. Clim. Change* **6**, 936–940 (2016). doi: [10.1038/nclimate3058](https://doi.org/10.1038/nclimate3058)
85. B. D. Santer *et al.*, Causes of differences in model and satellite tropospheric warming rates. *Nat. Geosci.* **10**, 478–485 (2017). doi: [10.1038/ngeo2973](https://doi.org/10.1038/ngeo2973)
86. M. Collins *et al.*, in *Climate Change 2013: The Physical Science Basis. Contribution of Working Group I to the Fifth Assessment Report of the Intergovernmental Panel on Climate Change*, T. F. Stocker *et al.*, Eds. (Cambridge Univ. Press, 2013), pp. 867–952.
87. P. C. Taylor *et al.*, A decomposition of feedback contributions to polar warming amplification. *J. Clim.* **26**, 7023–7043 (2013). doi: [10.1175/JCLI-D-12-00696.1](https://doi.org/10.1175/JCLI-D-12-00696.1)
88. G. Flato *et al.*, in *Climate Change 2013: The Physical Science Basis. Contribution of Working Group I to the Fifth Assessment Report of the Intergovernmental Panel on Climate Change*, T. F. Stocker *et al.*, Eds. (Cambridge Univ. Press, 2013), pp. 741–866.
89. Q. Shu, Z. Song, F. Qiao, Assessment of sea ice simulations in CMIP5. *Cryosphere* **9**, 399–409 (2015). doi: [10.5194/tc-9-399-2015](https://doi.org/10.5194/tc-9-399-2015)
90. J. A. Screen, C. Deser, I. Simmonds, Local and remote controls on observed Arctic warming. *Geophys. Res. Lett.* **39**, L10709 (2012). doi: [10.1029/2012GL051598](https://doi.org/10.1029/2012GL051598)
91. I. Cvijanovic *et al.*, Future loss of Arctic sea-ice cover could drive a substantial decrease in California's rainfall. *Nat. Commun.* **8**, 1947 (2017). pmid: [29209024](https://pubmed.ncbi.nlm.nih.gov/29209024/)
92. J. Hansen, L. Nazarenko, Soot climate forcing via snow and ice albedos. *Proc. Natl. Acad. Sci. U.S.A.* **101**, 423–428 (2004). doi: [10.1073/pnas.2237157100](https://doi.org/10.1073/pnas.2237157100); pmid: [14699053](https://pubmed.ncbi.nlm.nih.gov/14699053/)
93. Q. Ding *et al.*, Influence of high-latitude atmospheric circulation changes on summertime Arctic sea ice. *Nat. Clim. Change* **7**, 289–295 (2017). doi: [10.1038/nclimate3241](https://doi.org/10.1038/nclimate3241)
94. S. Solomon *et al.*, Mirrored changes in Antarctic ozone and stratospheric temperature in the late 20th versus early 21st centuries. *J. Geophys. Res.* **122**, 8940–8950 (2017). doi: [10.1002/2017JD026719](https://doi.org/10.1002/2017JD026719)
95. B. D. Santer *et al.*, Separating signal and noise in atmospheric temperature changes: The importance of timescale. *J. Geophys. Res.* **116**, D22105 (2011). doi: [10.1029/2011JD016263](https://doi.org/10.1029/2011JD016263)
96. B. D. Santer *et al.*, Human and natural influences on the changing thermal structure of the atmosphere. *Proc. Natl. Acad. Sci. U.S.A.* **110**, 17235–17240 (2013). doi: [10.1073/pnas.1305332110](https://doi.org/10.1073/pnas.1305332110); pmid: [24043789](https://pubmed.ncbi.nlm.nih.gov/24043789/)
97. J.-P. Vernier *et al.*, Major influence of tropical volcanic eruptions on the stratospheric aerosol layer during the last decade. *Geophys. Res. Lett.* **38**, L12807 (2011). doi: [10.1029/2011GL047563](https://doi.org/10.1029/2011GL047563)
98. J. C. Fyfe, K. von Salzen, J. N. S. Cole, N. P. Gillett, J.-P. Vernier, Surface response to stratospheric aerosol changes in a coupled atmosphere-ocean model. *Geophys. Res. Lett.* **40**, 584–588 (2013). doi: [10.1002/grl.50156](https://doi.org/10.1002/grl.50156)
99. R. R. Neely III *et al.*, Recent anthropogenic increases in SO<sub>2</sub> from Asia have minimal impact on stratospheric aerosol. *Geophys. Res. Lett.* **40**, 999–1004 (2013). doi: [10.1002/grl.50263](https://doi.org/10.1002/grl.50263)
100. G. Kopp, J. L. Lean, A new, lower value of total solar irradiance: Evidence and climate significance. *Geophys. Res. Lett.* **38**, L01706 (2011). doi: [10.1029/2010GL045777](https://doi.org/10.1029/2010GL045777)
101. R. E. Swanson, Evidence of possible sea-ice influence on Microwave Sounding Unit tropospheric temperature trends in polar regions. *Geophys. Res. Lett.* **30**, 2040 (2003). doi: [10.1029/2003GL017938](https://doi.org/10.1029/2003GL017938)
102. S. Manabe, R. T. Wetherald, R. J. Stouffer, Summer dryness due to an increase of atmospheric CO<sub>2</sub> concentration. *Clim. Change* **3**, 347–386 (1981). doi: [10.1007/BF02423242](https://doi.org/10.1007/BF02423242)
103. R. T. Wetherald, S. Manabe, The mechanisms of summer dryness induced by greenhouse warming. *J. Clim.* **8**, 3096–3108 (1995). doi: [10.1175/1520-0442\(1995\)008<3096:TMOSDI>2.0.CO;2](https://doi.org/10.1175/1520-0442(1995)008<3096:TMOSDI>2.0.CO;2)
104. H. Douville, M. Plazzotta, Midlatitude summer drying: An underestimated threat in CMIP5 models? *Geophys. Res. Lett.* **44**, 9967–9975 (2017). doi: [10.1002/2017GL075353](https://doi.org/10.1002/2017GL075353)
105. F. Cheruy, J. L. Dufresne, F. Hourdin, A. Ducharme, Role of clouds and land-atmosphere coupling in midlatitude continental summer warm biases and climate change amplification in CMIP5 simulations. *Geophys. Res. Lett.* **41**, 6493–6500 (2014). doi: [10.1002/2014GL061145](https://doi.org/10.1002/2014GL061145)
106. P. H. Stone, J. H. Carlson, Atmospheric lapse rate regimes and their parameterization. *J. Atmos. Sci.* **36**, 415–423 (1979). doi: [10.1175/1520-0469\(1979\)036<0415:ALRRAT>2.0.CO;2](https://doi.org/10.1175/1520-0469(1979)036<0415:ALRRAT>2.0.CO;2)
107. D. M. W. Frierson, J. Lu, G. Chen, Width of the Hadley cell in simple and comprehensive general circulation models. *Geophys. Res. Lett.* **34**, L18804 (2007). doi: [10.1029/2007GL031115](https://doi.org/10.1029/2007GL031115)
108. J. Bando, S. Solomon, A. Donohoe, D. W. J. Thompson, B. D. Santer, Influences of the Antarctic ozone hole on Southern Hemisphere summer climate change. *J. Clim.* **27**, 6245–6264 (2014). doi: [10.1175/JCLI-D-13-00698.1](https://doi.org/10.1175/JCLI-D-13-00698.1)
109. X.-W. Quan, M. P. Hoerling, J. Perlwitz, H. F. Diaz, T. Xu, How fast are the tropics expanding? *J. Clim.* **27**, 1999–2013 (2014). doi: [10.1175/JCLI-D-13-00287.1](https://doi.org/10.1175/JCLI-D-13-00287.1)
110. N. P. Gillett, T. D. Kell, P. D. Jones, Regional impacts of the southern annular mode. *Geophys. Res. Lett.* **33**, L23704 (2004). doi: [10.1029/2006GL027721](https://doi.org/10.1029/2006GL027721)
111. D. W. J. Thompson *et al.*, Signatures of the Antarctic ozone hole in southern hemisphere surface climate change. *Nat. Geosci.* **4**, 741–749 (2011). doi: [10.1038/ngeo1296](https://doi.org/10.1038/ngeo1296)
112. Q. Fu, C. M. Johanson, J. M. Wallace, T. Reichler, Enhanced mid-latitude tropospheric warming in satellite measurements. *Science* **312**, 1179 (2006). doi: [10.1126/science.1125566](https://doi.org/10.1126/science.1125566); pmid: [16728633](https://pubmed.ncbi.nlm.nih.gov/16728633/)
113. D. J. Seidel, W. J. Randel, Recent widening of the tropical belt: Evidence from tropopause observations. *J. Geophys. Res.* **112**, D20113 (2007). doi: [10.1029/2007JD008861](https://doi.org/10.1029/2007JD008861)
114. Y. Y. Hu, Q. Fu, Observed poleward expansion of the Hadley circulation since 1979. *Atmos. Chem. Phys.* **7**, 5229–5236 (2007). doi: [10.5194/acp-7-5229-2007](https://doi.org/10.5194/acp-7-5229-2007)
115. O. Heffernan, The mystery of the expanding tropics. *Nature* **530**, 20–22 (2016). doi: [10.1038/530020a](https://doi.org/10.1038/530020a); pmid: [26842039](https://pubmed.ncbi.nlm.nih.gov/26842039/)
116. I. M. Held, “The General Circulation of the Atmosphere” (2000); [www.whoi.edu/files/server.do?fileid=21464&pt=10&p=17332](http://www.whoi.edu/files/server.do?fileid=21464&pt=10&p=17332).
117. S. M. Kang, J. Lu, Expansion of the Hadley Cell under global warming: Winter versus summer. *J. Clim.* **25**, 8387–8393 (2012). doi: [10.1175/JCLI-D-12-00323.1](https://doi.org/10.1175/JCLI-D-12-00323.1)
118. U.S. Senate Environment and Public Works Committee Hearing, “Nomination of Attorney General Scott Pruitt to be Administrator of the U.S. Environmental Protection Agency,” 18 January 2017; [www.epw.senate.gov/public/\\_cache/files/6d95005c-bd1a-4779-af7e-be831db6866a/scott-pruitt-qfr-responses-01.18.2017.pdf](http://www.epw.senate.gov/public/_cache/files/6d95005c-bd1a-4779-af7e-be831db6866a/scott-pruitt-qfr-responses-01.18.2017.pdf).
119. J. A. Curry, Testimony in Hearing Before the Committee on Science, Space and Technology, House of Representatives, 29 March 2017; <https://science.house.gov/sites/republicans.science.house.gov/files/documents/HHRG-115-SY-WState-JCurry-20170329.pdf>.

## ACKNOWLEDGMENTS

We acknowledge the World Climate Research Programme's Working Group on Coupled Modelling, which is responsible for CMIP, and we thank the climate modeling groups for producing and making available their model output. For CMIP, the U.S. Department of Energy's Program for Climate Model Diagnosis and Intercomparison (PCMDI) provided coordinating support and led



development of software infrastructure in partnership with the Global Organization for Earth System Science Portals. We thank M. MacCracken (Climate Institute) and two reviewers for helpful comments. **Funding:** Work at LLNL was performed under the auspices of the U.S. Department of Energy under contract DE-AC52-07NA27344 through the Regional and Global Model Analysis Program (B.D.S., S.P.-C., M.D.Z., P.J.D., and J.P.) and the Early Career Research Program Award SCW1295 (I.C., C.B.). Additional support was provided by the LLNL-LDRD Program under project no. 13-ERD-032 (B.D.S., I.C., and C.B.); the Lee and Geraldine Martin Professorship at MIT (S.S.); NASA grant NNH12CF05C (F.J.W. and C.M.); and NASA grant NNX13AN49G

(Q.F.). **Author contributions:** B.D.S., I.C., and C.B. conceived the study; B.D.S., S.P.-C., and I.C. performed statistical analyses; J.P. calculated synthetic satellite temperatures from model simulation output; C.M., F.J.W., and C.-Z.Z. provided satellite temperature data; and all authors contributed to the writing and revision of the manuscript. **Competing interests:** None. **Data and materials availability:** All primary satellite and model temperature datasets used here are publicly available. Derived products (synthetic satellite temperatures calculated from model simulations) are provided at <https://pcmdi.llnl.gov/research/DandA/>. Disclaimer: The views, opinions, and findings contained in this report are those of the authors and should not be construed as a position, policy,

or decision of the U.S. Government, the U.S. Department of Energy, or the National Oceanic and Atmospheric Administration.

#### SUPPLEMENTARY MATERIALS

[www.sciencemag.org/content/361/6399/eaas8806/suppl/DC1](http://www.sciencemag.org/content/361/6399/eaas8806/suppl/DC1)

Materials and Methods

Supplementary Text

Figs. S1 to S13

References (120–127)

8 January 2018; accepted 7 June 2018

10.1126/science.aas8806